

A predictive mechanism for dynamic strain ageing in aluminium–magnesium alloys

WILLIAM A. CURTIN^{1*}, DAVID L. OLMSTED^{1†} AND LOUIS G. HECTOR Jr²

¹Division of Engineering, Brown University, Providence, Rhode Island 02912, USA

²General Motors Technical Center, 30500 Mound Rd., Warren, Michigan 48090-9055, USA

[†]Current address: Sandia National Laboratories, Albuquerque, New Mexico 87185-1411, USA

*e-mail: curtin@engin.brown.edu

Published online: 22 October 2006; doi:10.1038/nmat1765

Dynamic strain ageing (DSA) is the phenomenon in which solute atoms diffuse around dislocations and retard dislocation motion, leading to negative strain-rate sensitivity (nSRS) and thus to material instabilities during processing, an important issue in commercial metal alloys. Here, we show the mechanism of DSA and nSRS on experimental strain-rate, temperature and stress scales for Al–Mg to be single-atomic-hop motion of solutes from the compression to the tension side of a dislocation core. We derive an analytic expression for the strengthening versus strain rate and temperature that justifies widely used phenomenological forms, provides specific dependences of the parameters on material properties and is supported by atomistic kinetic Monte Carlo simulations. Using literature material properties, the predicted strengthening quantitatively agrees with the experimentally derived behaviour of Al–2.5% Mg at 300 K, and qualitatively agrees with the strain rate and temperature ranges of DSA and nSRS in Al–Mg alloys. The analyses herein show a clear path for multiscale design, from quantum to continuum mechanics, of solute strengthening in face-centred-cubic metal alloys.

The change in material strength τ versus the change in strain rate $\dot{\epsilon}$ is the strain-rate sensitivity, $m = d(\ln \tau)/d(\ln \dot{\epsilon})$. The strain-rate sensitivity plays a key role in material processing and formability. Negative strain-rate sensitivity (nSRS, $m < 0$) in metal alloys generates instabilities during deformation and forming, because a local increase in strain rate softens the material locally. nSRS is manifested macroscopically in serrated stress–strain behaviour and Portevin–LeChatelier deformation bands, both of which are highly detrimental for material fabrication. Identifying the mechanisms of nSRS and devising alloy-design strategies to modify the nSRS behaviour are therefore important objectives for using many alloys in a wide range of manufacturing processes.

In solute-strengthened alloys, such as the 5XXX Al–Mg alloys, nSRS is attributed to the diffusion of substitutional solutes towards the dislocations (dynamic strain ageing or DSA). The diffusion is driven by the enthalpy change $p\Delta V$, where ΔV is the solute misfit volume and p is the dislocation pressure field, lowering the total energy and making dislocation motion more difficult^{1,2}. Lower $\dot{\epsilon}$ or higher temperatures T leads to more diffusion, faster strengthening of dislocations, a stronger material and thus nSRS.

Bulk solute diffusion around a static dislocation is well established in continuum models^{1,3–6}. Using the continuum pressure field for an edge dislocation,

$$p(x, y) = \frac{(1 + \nu)\mu b}{3(1 - \nu)\pi} y / (x^2 + y^2)$$

with Burgers vector b , shear modulus μ and Poisson's ratio ν , the change in core solute concentration versus time, t , is

$$\Delta c^{\text{cont}}(t) = c(t) - c_0 = (f - c_0)(1 - e^{-(t/t^*)^{2/3}}) \quad (1a)$$

$$t^* = (\sqrt{2}b^2/D_b\beta W)(f/3c_0)^{3/2}, \quad (1b)$$

where c_0 is the bulk solute concentration, D_b the bulk solute diffusion coefficient, $W \approx |p(x = 0, y = \pm b)\Delta V|$ the maximum solute binding energy, $\beta = 1/kT$, and $f = c_0 e^{\beta W}/(1 + c_0 e^{\beta W})$ the saturation concentration. The diffusion coefficient is $D_b = 2b^2\nu_0 e^{-\beta\Delta H_b}$, where ΔH_b is the activation enthalpy and ν_0 the attempt frequency. Note that the pressure is singular and changes

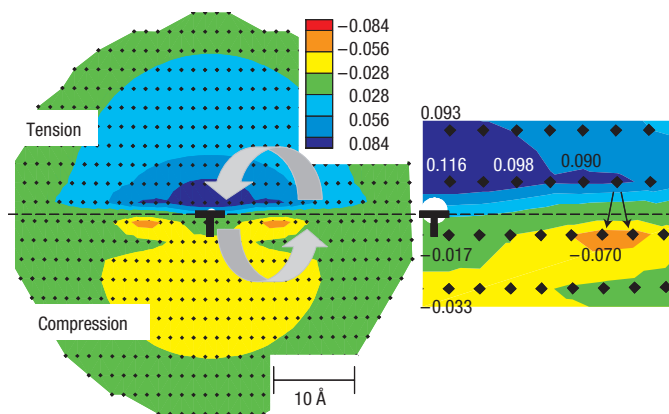


Figure 1 Binding energy of a Mg substitutional solute and an edge dislocation in Al versus Mg solute position. Contours in eV; positive energies indicate binding, that is lower total energy. Cores of the split partials are evident on the compression side of the dislocation²⁴. Arrows denote flux of solutes around the dislocation core in traditional continuum models. Right: magnification of the core region, with specific binding energies as indicated in eV, and arrows indicating the two cross-core transitions for which the activation enthalpy has been computed in ref. 19.

sign at $y = 0$, precluding continuum treatment of diffusion within the core.

Connecting solute diffusion to DSA and nSRS requires further approximations and assumptions. The form of equation (1a) is assumed to apply to a time-dependent extra strength $\Delta\tau_s(t)$ (resolved shear stress to move the dislocation) of

$$\Delta\tau_s(t) = \Delta\tau_0(1 - e^{-(t/t^*)^n}), \quad n = 2/3. \quad (2)$$

Solute diffusion occurs over the waiting time t_w when dislocations are pinned at obstacles^{7–10}. t_w is related to the strain rate via $t_w = \Omega/\dot{\epsilon}$, where $\Omega = \rho_m b / \sqrt{\rho_f} \approx 10^{-4} - 10^{-3}$, and ρ_m and ρ_f are the mobile and forest dislocation densities^{9–16}. Setting $t = t_w = \Omega/\dot{\epsilon}$ in equation (2) and defining $\dot{\epsilon}^* = \Omega/t^*$ then leads to a strain-rate-dependent strengthening of

$$\Delta\tau_s(\dot{\epsilon}) = \Delta\tau_0(1 - e^{-(\dot{\epsilon}^*/\dot{\epsilon})^n}), \quad n = 2/3. \quad (3)$$

$\Delta\tau_0$ and $\dot{\epsilon}^*$, and sometimes n , are then treated as fitting parameters^{15,16}. Equation (3) predicts nSRS by construction, as anticipated by Penning¹⁷. Use of equation (3) with $\Delta\tau_0 = 12$ MPa and $\dot{\epsilon}^* = 5 \times 10^{-5} \text{ s}^{-1}$ at 300 K in a homogenized crystal plasticity model leads to the prediction of serrated flow and the various types of macroscopic Portevin–LeChatelier band versus strain rate observed in an Al–2.5% Mg alloy¹⁶. This is strong evidence that the phenomenological form of equation (3) is basically correct.

The standard model of equation (3) suffers from fundamental problems on deeper inspection. First, $\dot{\epsilon}^*$ for vacancy-assisted diffusion of Mg in Al is many orders of magnitude smaller than experimentally derived values. With $\Delta H_b = 1.19$ eV and $\nu_0 = 3.8 \times 10^{13} \text{ s}^{-1}$ (ref. 18), $\dot{\epsilon}^*$ at 300 K for $c_0 = 2.5\%$ (using $W = 0.08$ eV and $\Omega = 0.00063$, see below) is $\approx 4 \times 10^{-11} \text{ s}^{-1}$, a discrepancy of $\approx 10^6$ with experiments. Pipe diffusion along the dislocation core¹⁹ or other recent models^{20,21} do not rectify this discrepancy. Second, the strength of a fully formed solute cloud is also much too large, 500–5,000 MPa (refs 1,5,22,23), and the binding energy formally diverges¹. Our finite-size simulations here confirm the previous literature, with strengths ~ 300 MPa and binding energies of ~ 50 eV. Third, there is only very weak

theoretical justification for the leap from equation (1) to (2) (ref. 8). Fourth, equations (2) and (3) assume that strength is an additive quantity, which is not generally true. Thus, no existing models are predictive at the materials level, and so a quantitatively accurate understanding of the mechanisms of DSA in Al–Mg does not yet exist.

Here, we demonstrate that the mechanism of DSA and nSRS on experimentally measured strain rate and stress scales is the single-atomic jump of solutes directly across the slip plane, from the compression to the tension side, in the core of the dislocation. This ‘cross-core’ diffusion mechanism is outside the scope of continuum models, has a strong thermodynamic driving force due to the large enthalpy difference between solutes on either side of the slip plane in the core, has an activation enthalpy much lower than in the bulk¹⁹, leads to an additive strengthening in the form of equations (2) and (3), but with $n = 1$, and connects the parameters in equations (2) and (3) with fundamental solute–dislocation interactions. Moreover, using literature material parameters for Al–Mg, this mechanism has strengths of ~ 10 –20 MPa, binding energies of ~ 1 –2 eV, and quantitatively agrees with the experiments on Al–Mg over a range of concentrations and temperatures^{16,24,25}. Our new picture of the DSA and nSRS phenomena quantitatively addresses all the issues sidestepped in previous models and puts the phenomenon and the widely used equation (3) on a firm theoretical materials science foundation. The new model also points towards quantitative multiscale modelling for the design of new alloy systems via first-principles computations of solute/dislocation-core interaction and diffusion enthalpies.

Figure 1 shows the binding energy $E^*(x_i, y_i)$ between a single substitutional Mg at in-plane position (x_i, y_i) and an edge dislocation ($b = 2.851$ Å) at the origin, computed by molecular statics^{19,26} (see the Methods section) the energy is independent of the z coordinate. Across a core interaction region of width $w \approx 7.5b = 21$ Å, there is a differential binding energy of $\Delta W \sim 0.13 \pm 0.02$ eV (positive values denote binding), which provides a strong driving force for direct transport of solute atoms across the slip plane. Differences in energy among other neighbouring sites are notably smaller. The contours of energy in Fig. 1 show the standard pathways for bulk diffusion in continuum models: away from the compression side and into the tension side of the core.

ΔH values for vacancy-assisted Mg migration around the core have been computed¹⁹. There are reported values, 0.977 and 1.1 eV, for the two transitions indicated in Fig. 1 corresponding to Mg moving across the core from tension to compression against the thermodynamic driving force ΔW . These values correspond to $\Delta H_c + \Delta W/2$, where $\Delta H_c \approx 0.97$ eV is the average activation enthalpy for transitions from tension to compression and vice versa, consistent with our independent calculations. This value is significantly lower than the activation enthalpy $\Delta H_b = 1.20$ eV for bulk diffusion computed by the same method. Migration paths perpendicular to the plane of the core on either the tension or compression side quickly attain the bulk value¹⁹.

The above energetic and kinetic considerations show that the cross-core diffusion has both a larger thermodynamic driving force and a reduced diffusion activation enthalpy relative to regions outside the core. On this basis, we now model the solute motion directly across the slip plane in the core and its consequences for time-dependent dislocation binding energy and strengthening.

Ignoring the small variations in cross-core energy difference along the core, let the solute concentrations on the core tension and compression planes be $c_t(t)$ and $c_c(t)$, and the average binding-energy difference between these sites be $\overline{\Delta W}$. Each site has three neighbours on the opposite side of the slip plane. Denoting a reference core transition rate as $\Gamma_c = \nu_0 e^{-\beta \Delta H_c}$, the transition

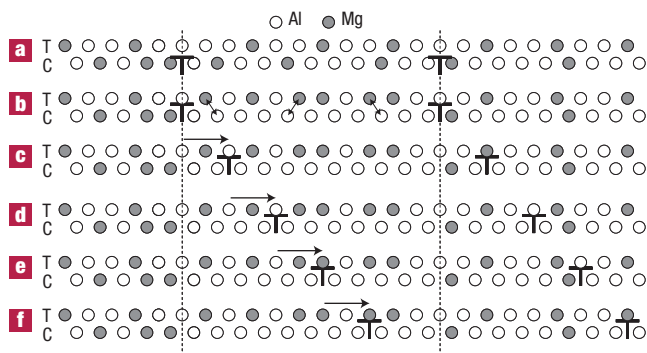


Figure 2 Schematic diagrams of the core solute positions relative to a dislocation being driven to the right by an applied stress. **a**, Before core diffusion; **b**, after core diffusion; **c–f**, under increasing applied stress. The core region moves away from the positions of the diffused solutes on the tension (T) plane and into a region of undiffused solutes randomly distributed on the tension (T) and compression (C) planes.

rate from tension to compression is $\Gamma_{t \rightarrow c} = 3\Gamma_c e^{-\beta \Delta \bar{W}/2}$ and that from compression to tension is $\Gamma_{c \rightarrow t} = 3\Gamma_c e^{+\beta \Delta \bar{W}/2}$; the ratio is $e^{\beta \Delta \bar{W}}$, as required by detailed balance. Solution of the relevant master equations $\dot{c}_t(t) = \Gamma_{c \rightarrow t} c_c(t) - \Gamma_{t \rightarrow c} c_t(t)$ and $\dot{c}_c(t) = \Gamma_{t \rightarrow c} c_t(t) - \Gamma_{c \rightarrow t} c_c(t)$, with initial conditions $c_c(0) = c_t(0) = c_0$, yields the concentration change on the tension side

$$\Delta c_t(t) = c_t(t) - c_0 = c_0 \tanh(\beta \Delta \bar{W}/2) \left[1 - e^{-6 \cosh(\beta \Delta \bar{W}/2) \Gamma_c t} \right]. \quad (4)$$

The dislocation-binding-energy change due to cross-core solute transport is then

$$\Delta E^{\text{core}}(t) = \Delta c_t(t) N \Delta \bar{W}, \quad (5)$$

where $N = 2w\xi/\sqrt{3}b^2$ is the number of atoms in the interaction core width w of a dislocation segment of length ξ on a (111) slip plane in a face-centred-cubic crystal.

Prediction of the strength change due to cross-core solute diffusion requires a model for the dislocation/solute-cloud energy $E(x, t, \tau)$ versus dislocation position x and applied stress τ . Starting at $x = 0$, the dislocation attempts to glide away from the core region $-w/2 \leq x \leq w/2$ under an applied stress. As Fig. 2 schematically shows, the energy changes because diffused solutes on the tension side are left behind as the core moves, whereas new undiffused solutes on both tension and compression sides enter the core region. Denoting the solute binding energy change at position x in the core by $\Delta W(x)$, the total energy is

$$E(x, t, \tau) = E_0(x) - \tau b \xi x - \sum_i \Delta W(x_i - x),$$

where the sum is over the diffused solutes $\{i\}$ at positions $\{-w/2 \leq x_i \leq w/2\}$, $E_0(x)$ is the energy well for the dislocation before any solute diffusion and $-\tau b \xi x$ is the work done by the applied stress. The time-dependent strength $\tau_s(t)$ is then the applied stress at which the energy barrier becomes zero or, equivalently, at which the energy versus position has no local minimum, $dE(x, t, \tau_s)/dx \leq 0$ for all $x \geq 0$. The strength is then

$$\tau_s(t) = \max_x \left[(dE_0(x)/dx)/b\xi + (1/b\xi) \sum_j d\Delta W(x_j - x)/dx \right]. \quad (6)$$

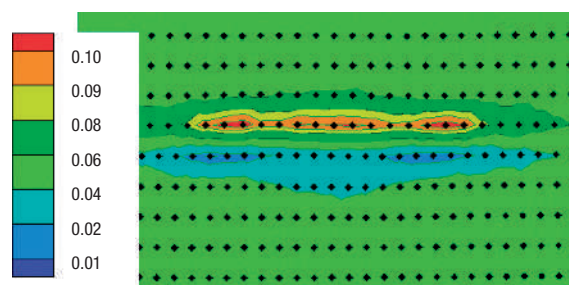


Figure 3 Contour map of Mg solute concentration after diffusion for a time $D_b t / 2b^2 = 0.18$ at 500 K as computed in the kMC model. Solute transport is predominantly across the slip plane from compression (bottom) to tension (top). Initial Mg concentration was 0.05 throughout the system.

Changing the sum to an integral, and noting that by symmetry $\Delta W(-x) = \Delta W(x)$, leads to

$$\tau_s(t) = \max_x \left[(dE_0(x)/dx)/b\xi + (2\Delta c_t(t)/\sqrt{3}b^3) \times [\Delta W(x - w/2) - \Delta W(x + w/2)] \right].$$

Approximating the solute binding energy outside the core as zero and a constant $\Delta \bar{W}$ within $-w/2 \leq x \leq w/2$ yields

$$\begin{aligned} \tau_s(t) &= dE_0(x)/dx|_{\text{max}}/b\xi + \alpha(2\Delta c_t(t)/\sqrt{3}b^3) \Delta \bar{W} \\ &= \tau_{s0} + \Delta \tau_s(t), \end{aligned} \quad (7)$$

where $\tau_{s0} = dE_0(x)/dx|_{\text{max}}/b\xi$ is the initial strength and $\Delta \tau_s(t) = \alpha(2\Delta c_t(t)/\sqrt{3}b^3) \Delta \bar{W}$ is an additive strengthening due to solute diffusion, with $\alpha = 1$. A more accurate result, recognizing that the initial strength is largely independent of the diffused solutes in the core, has $\alpha = \langle \Delta W(x - w/2) - \Delta W(x + w/2) \rangle_x / \Delta \bar{W}$, where $\langle \rangle_x$ denotes an average over the range of positions where $dE_0(x)/dx$ is maximized. Using equation (4) in (7) leads to our main result for the time-dependent additive strengthening,

$$\Delta \tau_s(t) = \alpha(2c_0 \Delta \bar{W} / \sqrt{3}b^3) \tanh(\beta \Delta \bar{W}/2) [1 - e^{-6 \cosh(\beta \Delta \bar{W}/2) \Gamma_c t}], \quad (8)$$

which is identical in form to equation (2) with

$$\begin{aligned} \Delta \tau_0 &= 2\alpha c_0 \Delta \bar{W} \tanh(\beta \Delta \bar{W}/2) / \sqrt{3}b^3 \approx 2\alpha c_0 \Delta \bar{W} / \sqrt{3}b^3 \\ t^* &= [6 \cosh(\beta \Delta \bar{W}/2) \Gamma_c]^{-1} \approx [3\nu_0 e^{-\beta(\Delta H_c - \Delta \bar{W}/2)}]^{-1} \\ n &= 1. \end{aligned} \quad (9)$$

Equation (3) follows by substituting $t = t_w = \Omega/\dot{\epsilon}$ and $\dot{\epsilon}^* = \Omega/t^*$ into equation (8). Equations (7)–(9) are the main results of this paper.

We now highlight key features of the above analysis. We find $\Delta c(t) \sim \Delta E(t) \sim \Delta \tau_s(t)$ without assumptions. Equations (7)–(9) predict that the strength change is additive to τ_{s0} . $\Delta \tau_0$ is governed by the material parameters c_0 , $\Delta \bar{W}$ and b , but not w . $t^* = [3\nu_0 e^{-\beta(\Delta H_c - \Delta \bar{W}/2)}]^{-1}$ and $\dot{\epsilon}^* = \Omega/t^*$ are governed by an effective activation enthalpy $\Delta H_c^{\text{eff}} = \Delta H_c - \Delta \bar{W}/2 \ll \Delta H_b$. The exponent in equation (2) is $n = 1$. The phenomenology of equations (2) and (3) is thus put on a firm theoretical foundation.

To explicitly show the cross-core mechanism and to support the analytic model, we use a kinetic Monte Carlo (kMC) model (see Methods). We do not take explicit account of the cross-core migration enthalpy ΔH_c ; all transitions use the bulk

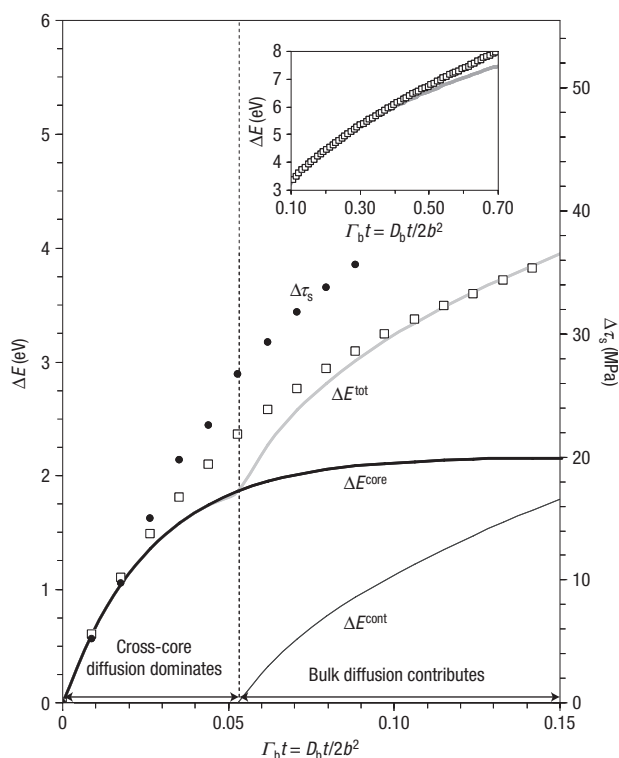


Figure 4 Change in binding energy (squares) and change in strength (circles) versus dimensionless time, as computed by kMC simulations at 300 K. Core and bulk activation enthalpies and transition rates are assumed equal ($\Delta H_b = \Delta H_c$, $\Gamma_b = \Gamma_c$) in these simulations. Also shown are predictions for the binding energy due to the cross-core diffusion mechanism equation (5), which dominates for $D_b t/2b^2 \leq (3e^{\beta \Delta W/2})^{-1} \approx 0.025$ (thick black line), the continuum bulk diffusion mechanism of equation (11) at longer times $D_b t/2b^2 > D_b t_{\min}^{\text{cont}}/2b^2 = (6\beta W)^{-1} \approx 0.055$ (thin black line) and the sum of the two (grey line). Inset: Simulated and predicted total energies versus time, to longer times.

migration enthalpy ΔH_b modified only by the thermodynamic driving force. Nonetheless, the large cross-core driving force $\Delta \bar{W}$ accelerates the cross-core diffusion sufficiently to separate the timescales for the cross-core and bulk mechanisms. Figure 3 shows the Mg concentration distribution at a time where the core diffusion is complete but the bulk diffusion has barely started; the concentration in the core on the first compressive slip plane is nearly 0%, whereas that on the first tensile slip plane is nearly doubled to 10%, with little change elsewhere.

Proceeding quantitatively, as diffusion occurs in the kMC model we compute the binding energy of the dislocation as a function of the virtual displacement x from its initial position $x=0$, by summing the individual Mg–dislocation energies as

$$E(x, t, \tau) = \sum_i E^s(x_i(t) - x, y_i(t)) - \tau b \xi x. \quad (10)$$

Equation (10) is accurate because Mg–Mg interactions are negligible, even in the core²⁶. As in equation (6), the time-dependent strength is computed as $\tau_s(t) = dE(x, t, 0)/dx|_{\max}/b\xi$. Figure 4 shows the change in binding energy $\Delta E(t) = E(0, t, \tau_0) - E(0, 0, \tau_0)$ and the change in strength $\Delta \tau_s(t) = \tau_s(t) - \tau_{s0}$ versus dimensionless time $\Gamma_b t = D_b t/2b^2$, obtained by averaging 100 kMC runs for each of six initial random Mg configurations at $c_0 = 5\%$ and 300 K. Consistent with the predictions of equations (4), (5) and (7), at early times $\Gamma_b t \leq (1/3e^{\beta \Delta W/2}) \approx 0.025$, where the cross-core

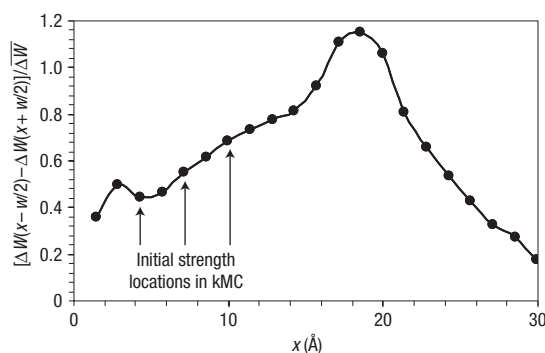


Figure 5 Strengthening parameter versus dislocation position during sliding. The positions of the static solute strengthening points in the kMC simulations are as indicated.

mechanism dominates, both energy and strength changes are linear in t , for example $\Delta E \sim t^n$, $n \sim 1$, indicating single-atomic-jump transport rather than the bulk diffusion ($n = 2/3$) of equations (1a) and (1b). The strength change is also independent of the initial values, implying that the strength change is approximately additive. Similar results are found at 500 K. At early times, where cross-core diffusion dominates, excellent quantitative agreement between the analytic model and the kMC simulations is obtained for the binding energy: Fig. 4 shows the prediction of equation (5) for $\Delta E^{\text{core}}(t)$, with $\Delta \bar{W} = 0.13$ eV and $w = 7.5b$ from Fig. 1, and with $\Gamma_c = \Gamma_b$, as used in the kMC. Good agreement is also found at 500 K using the same parameters.

The magnitude of the strengthening in the kMC is also in good agreement with our model. Equation (8) predicts a ratio of strength to binding energy of $\Delta \tau_s(t)/\Delta E(t) = \alpha/\xi b w$. Figure 5 shows the model prediction for $[\Delta W(x-w/2) - \Delta W(x+w/2)]/\Delta \bar{W}$ using the energies in the kMC model; the arrows indicate the positions of the original strengths in the kMC samples, for which the average is $\alpha = 0.56$. The model thus predicts $\Delta \tau_s(t)/\Delta E(t) = 13 \text{ MPa eV}^{-1}$, versus a kMC simulation value of 9 MPa eV^{-1} . The small discrepancy is probably due to the smearing and neglect of subtle details near $x = \pm w/2$ in the model and/or to small amounts of lateral diffusion in the kMC. A kMC study using the actual site-to-site activation enthalpies in and around the core should be carried out and compared with a more detailed analytic model before attempting to rectify the small differences.

At longer times, the qualitative and quantitative characteristics of the bulk continuum diffusion models emerge from the kMC simulations^{1,5,6,22,23}. The binding energy and strength continue to increase nearly in proportion, evolving towards a power law in time with $n \approx 2/3$, and the binding energy eventually reaches 50–100 eV and the strength ~ 300 MPa. The minimum time t_{\min}^{cont} at which continuum diffusion over distances $> b$ can occur is $D_b t_{\min}^{\text{cont}}/2b^2 \approx 1/6\beta W$ (ref. 5), after which the additional core concentration and binding energy can be estimated from equations (1a), (1b) and (5) as

$$\begin{aligned} \Delta c^{\text{cont}}(t) &= (f - c_0)(1 - e^{-((t-t_{\min}^{\text{cont}})/t^*)^{2/3}}), \\ \Delta E^{\text{cont}}(t) &= \Delta c^{\text{cont}}(t) N W, \quad t > t_{\min}^{\text{cont}}. \end{aligned} \quad (11)$$

The total binding-energy change is then $\Delta E^{\text{tot}}(t) \approx \Delta E^{\text{core}}(t) + \Delta E^{\text{cont}}(t)$ for $t > t_{\min}^{\text{cont}}$. Figure 4 shows the predicted $\Delta E^{\text{cont}}(t)$ and $\Delta E^{\text{tot}}(t)$ using $W = 0.08$ eV as a slightly adjustable parameter (theoretically, $W \approx \Delta \bar{W}/2$); very good agreement is obtained to long times (Fig. 4 inset). Results at 500 K using the same parameters are also good.

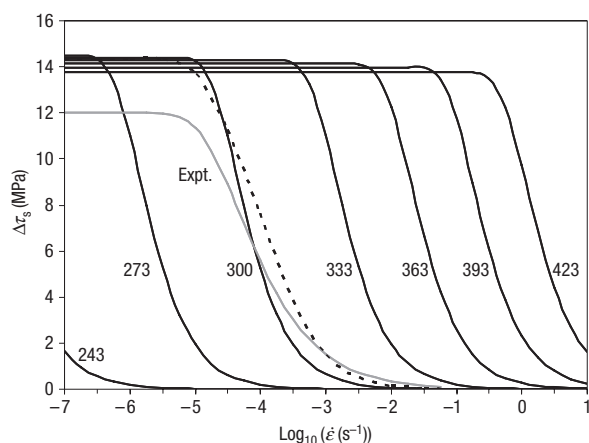


Figure 6 Strength change versus strain rate over a range of temperatures (in K) as predicted by equation (8) (black lines), with parameters given in the text. Also shown is the model of equation (3) at 300 K using parameters derived from experiments (grey line, ref. 16) and the prediction of the present model with a small spread in cross-core activation enthalpies at 300 K (dashed line).

We now show that the predictions of our mechanistically derived equations (7)–(9) are in excellent agreement with experiments. To predict the strengthening, we use $\Delta W = 0.13$ eV. A value $\alpha \approx 0.56$ is found by averaging over the spatial range where the static solute strengthening is typically found (Fig. 5). Equation (9) then predicts a strength prefactor of $\Delta\tau_0 = 14.5$ MPa, in excellent agreement with the experimentally derived value of 12 MPa reported in ref. 16 for $c_0 = 2.5\%$. To predict the timescale, we use $\Delta H_c = 0.97$ eV, $\Delta W = 0.13$ eV and the bulk attempt frequency $\nu_0 = 3.8 \times 10^{13} \text{ s}^{-1}$ (ref. 18). Equation (9) then predicts a characteristic time $t^* = 13.8$ s at 300 K. Using $\Omega = 0.00063$ as appropriate for a plastic strain of $\sim 15\%$ (ref. 15), around which the data in ref. 16 were fitted, the predicted characteristic strain rate is $\dot{\epsilon}^* = 4.5 \times 10^{-5} \text{ s}^{-1}$, nearly identical to the value reported in ref. 16. The accurate numerical predictions for both the strength and strain-rate scales are secondary to the fact that our model rectifies the large discrepancies of 50–500 and 10^6 , respectively, in the previous theories. Note that all parameters used here are from experiment, atomistic simulations or independent models (for example for Ω); there is no fitting.

Using the same parameters and $t = t_w$, $\dot{\epsilon} = \Omega/t_w$ and $\dot{\epsilon}^* = \Omega/t^*$ in equation (8) yields the predicted strengthening $\Delta\tau_s$ versus $\log_{10} \dot{\epsilon}$ for a range of temperatures as shown in Fig. 6. Our model predicts measurable DSA effects in the experimental range of strain rates (10^{-6} – 10^{-1} s^{-1}) over the experimental range of temperatures (233–353 K) (see, for example, refs 24,25). The fit in ref. 16 to equation (3) at 300 K is also shown; the agreement is very good. The difference in the breadth of strain rate is due to $n = 1$ versus $n = 2/3$; this can be rectified within our model by using a narrow range of $\Delta H_c \approx 0.92$ – 1.0 eV rather than a single value, as shown in Fig. 6.

Further implications of the cross-core diffusion mechanism are as follows. First, the mechanism can operate for all dislocation characters, including 0° screws, for which the continuum pressure is zero. The activation enthalpies and driving forces vary with character, with ΔH_c as low as 0.82 eV for 60° dislocations and over 1.0 eV for 0° (ref. 19), and with $\Delta W \approx 0.07$ eV for 0° (ref. 26). This may further broaden the range of strain rate at fixed temperature. Second, the mechanism has implications for solute-drag creep at higher temperatures and low stresses. Third, the mechanism can

be included in 3D discrete dislocation simulations that include dislocation junction creation and annihilation, bowing, forest hardening and pile-ups^{27–30}.

In summary, the cross-core model provides a physical justification of a widely used phenomenological model for DSA, shows that the DSA behaviour depends on only a limited number of fundamental material parameters and makes accurate predictions for the strength and strain-rate parameters in application to Al–Mg. All of the key material parameters can be computed with higher fidelity via quantum-mechanical calculations of solute–dislocation configurations. The present model and methods therefore provide the framework within which first-principles data for Al or other face-centred-cubic metal alloys containing a range of elemental solute additions can be used to predict dynamic strain ageing phenomena.

METHODS

We study Al alloyed with Mg as a substitutional solute using well calibrated embedded-atom-method potentials for the Al, Mg and Al/Mg interactions^{31–33}. We model a straight edge dislocation with line direction along \hat{z} and $b = 2.85$ Å along \hat{x} , as in previous analyses^{1,3–16,22,23}, in a simulation cell of size $X = 114$ Å, $Y = 91.8$ Å, $Z = \xi = 113.4$ Å that is periodic in X and Z (refs 26,34). This dislocation dissociates approximately into two partial dislocations, separated by a stacking fault of width ≈ 15 Å. This width is slightly larger than expected in real Al, but scales out of the calculations of strengthening. The width is independent of Mg concentration in the core in the concentration range relevant here ($< 10\%$; ref. 26). We appropriately choose the segment length, important for total energies, as $\xi \sim (Adb^{3/2}/Wc_0^{1/2})^{2/3}$, where A is the line tension and $d \sim 10$ – 20 Å is an effective range of dislocation/solute interactions; segments smaller than ξ remain straight^{35,36}.

We computed our Mg migration enthalpies using the ridge–saddle method³⁷. These calculations and those in ref. 19 include full relaxation of the simulation cell during the search for the transition state.

We carried out the kMC simulations as follows. In a simulation cell containing an initial random distribution of $c_0 = 5$ at.% Mg atoms, we place the dislocation at a location denoted $x = 0$, where Mg concentration fluctuations pin the dislocation with initial strengths in the range $\tau_{s0} \sim 45$ – 90 MPa (ref. 26). We apply a small initial stress of $\tau_0 = 15$ MPa. We then model diffusion of Mg atoms by a vacancy mechanism, by successive exchanges of Mg with neighbouring Al atoms, following the standard kMC methodology³⁸. Because only very few site-to-site cross-core activation enthalpies have been computed previously and obtaining them all is a daunting task, and to illustrate the effects of both cross-core diffusion and the traditional bulk solute diffusion within one simulation, we use the bulk activation enthalpy ΔH_b , which includes the vacancy formation enthalpy, for all kMC transitions, adjusted so that the proper ratio of reverse and forward transition rates is maintained. Specifically, the transition rate of Mg from site i to neighbouring site j is $\Gamma_{i \rightarrow j} = \nu_0 e^{-\beta(\Delta H_b - \Delta W_{ij}/2)} = \Gamma_b e^{\beta \Delta W_{ij}/2}$, where $\Delta W_{ij} = W(x_i) - W(x_j)$ is the binding-energy difference for Mg between sites i and j (see Fig. 1). The Mg site energies, precomputed by molecular statics, include full relaxation of the atomistic system. The corresponding bulk continuum diffusion coefficient is $D_b = 2b^2 \Gamma_b$.

Received 24 April 2006; accepted 15 September 2006; published 22 October 2006.

References

- Hirth, J. P. & Lothe, J. *Theory of Dislocations* 2nd edn (Wiley, New York, 1982).
- Robinson, J. M. & Shaw, M. P. Microstructural and mechanical influences on dynamic strain ageing phenomena. *Int. Mater. Rev.* **39**, 113–122 (1994).
- Cottrell, A. H. & Bilby, B. A. Dislocation theory of yielding and strain ageing of iron. *Proc. R. Soc. A* **62**, 49–62 (1949).
- Cottrell, A. H. Theory of brittle fracture in steel and similar metals. *Trans. Met. Soc. AIME* **212**, 192–203 (1958).
- Friedel, J. *Dislocations* (Addison-Wesley, New York, 1964).
- Louat, N. On the theory of the Portevin–Le Châtelier effect. *Scripta Metall.* **15**, 1167–1170 (1981).
- McCormick, P. G. A model for the Portevin–Le Châtelier effect in substitutional alloys. *Acta Metall.* **20**, 351–354 (1972).
- van den Beukel, A. Theory of the effect of dynamic strain ageing on mechanical properties. *Phys. Status Solidi A* **30**, 197–206 (1975).

9. Estrin, Y. & Kubin, L. P. Collective dislocation behaviour in dilute alloys and the Portevin-Le Châtelier effect. *J. Mech. Behav. Mater.* **2**, 255–292 (1989).
10. Kubin, L. P. & Estrin, Y. Evolution of dislocation densities and the critical conditions for the Portevin-Le Châtelier effect. *Acta Metall. Mater.* **38**, 697–708 (1990).
11. Kubin, L. P. & Estrin, Y. The critical conditions for jerky flow: discussion and application to Cu-Mn solid solutions. *Phys. Status Solidi B* **172**, 173–185 (1992).
12. Estrin, Y. & Kubin, L. P. in *Continuum Models for Materials with Microstructure* (ed. Mühlhaus, H. B.) 395–450 (Wiley, Chichester, 1995).
13. Lebyodkin, M., Dunin-Barkovskii, L., Bréchet, Y., Kubin, L. & Estrin, Y. Kinetics and statistics of jerky flow: experiments and computer simulations. *Mater. Sci. Eng. A* **234–236**, 115–118 (1997).
14. Lebyodkin, M., Dunin-Barkovskii, L., Bréchet, Y., Estrin, Y. & Kubin, L. P. Spatio-temporal dynamics of the Portevin-Le Châtelier effect: experiment and modelling. *Acta Mater.* **48**, 2529–2541 (2000).
15. Zhang, S., Estrin, Y. & McCormick, P. G. The morphology of Portevin-Le Châtelier bands: finite element simulation for Al-Mg-Si. *Acta Mater.* **49**, 1087–1094 (2001).
16. Kok, S. *et al.* Spatial coupling in jerky flow using polycrystal plasticity. *Acta Mater.* **51**, 3651–3662 (2003).
17. Penning, P. Mathematics of the Portevin-Le Châtelier effect. *Acta Metall.* **20**, 1169–1175 (1972).
18. Fujikawa, S. & Hirano, K. Diffusion of ^{28}Mg in aluminum. *Mater. Sci. Eng.* **27**, 25–33 (1977).
19. Picu, R. C. & Zhang, D. Atomistic study of pipe diffusion in Al-Mg alloys. *Acta Mater.* **52**, 161–171 (2004).
20. Picu, R. C. A mechanism for the negative strain-rate sensitivity of dilute solid solutions. *Acta Mater.* **52**, 3447–3458 (2004).
21. Rizzi, E. & Hahnner, P. On the Portevin-Le Chatelier effect: theoretical modeling and numerical results. *Int. J. Plast.* **20**, 121–165 (2004).
22. Barnett, D. M., Oliver, W. C. & Nix, W. D. The binding force between an edge dislocation and a Fermi-Dirac solute atmosphere. *Acta Metall.* **30**, 673–678 (1982).
23. Barnett, D. M., Wong, G. & Nix, W. D. The binding force between a Peierls-Nabarro edge dislocation and a Fermi-Dirac solute atmosphere. *Acta Metall.* **30**, 2035–2041 (1982).
24. Klose, F. B. *et al.* Analysis of Portevin-Le Chatelier serrations of type B in Al-Mg. *Mater. Sci. Eng. A* **369**, 76–81 (2004).
25. Picu, R. C. *et al.* Strain rate sensitivity of the commercial aluminum alloy AA5182-O. *Mater. Sci. Eng. A* **390**, 334–343 (2005).
26. Olmsted, D., Curtin, W. A. & Hector, L. G. Molecular dynamics study of solute strengthening in Al/Mg alloys. *J. Mech. Phys. Solids* **54**, 1763–1788 (2006).
27. Fivel, M. C., Gosling, T. J. & Canova, G. R. Implementing image stresses in a 3D dislocation simulation. *Model. Simul. Mater. Sci. Eng.* **4**, 581–596 (1996).
28. Hiratani, M., Zbib, H. M. & Khaleel, M. A. Modeling of thermally activated dislocation glide and plastic flow through local obstacles. *Int. J. Plast.* **19**, 1271–1296 (2003).
29. Amodeo, R. J. & Ghoniem, N. M. Dislocation dynamics. I. A proposed methodology for deformation micromechanics. *Phys. Rev. B* **41**, 6958–6967 (1990).
30. Devincere, B. & Condat, M. Model validation of a 3D simulation of dislocation dynamics. *Acta Metall. Mater.* **40**, 2629–2637 (1992).
31. Ercolessi, F. & Adams, J. B. Interatomic potentials from first-principles calculations: the force matching method. *Europhys. Lett.* **26**, 583–588 (1994).
32. Liu, X.-Y., Adams, J. B., Ercolessi, F. & Moriarty, J. A. EAM potential for magnesium from quantum mechanical forces. *Model. Simul. Mater. Sci. Eng.* **4**, 293–303 (1996).
33. Liu, X.-Y., Ohotnicky, P. P., Adams, J. B., Rohrer, C. L. & Hyland, R. W. Anisotropic surface segregation in Al-Mg alloys. *Surf. Sci.* **373**, 357–370 (1997).
34. Olmsted, D. L., Hector, L. G., Curtin, W. A. & Clifton, R. J. Atomistic simulations of dislocation mobility in Al, Ni and Al/Mg alloys. *Model. Simul. Mater. Sci. Eng.* **13**, 371–388 (2005).
35. Labusch, R., Ahearn, J., Grange, G. & Haasen, P. in *Rate Processes in Plastic Deformation: Proceedings from the John E. Dorn Symposium* Vol 56 (eds Dorn, J. E., Li, J. C. M. & Mukherjee, A. K.) (American Society for Metals, Metals Park, Ohio, 1975).
36. Zaiser, M. Dislocation motion in a random solid solution. *Phil. Mag. A* **82**, 2869–2883 (2002).
37. Ionova, I. V. & Carter, E. A. Ridge method for finding saddle points on potential energy surfaces. *J. Chem. Phys.* **98**, 6377–6386 (1993).
38. Voter, A. F. in *Radiation Effects in Solids* (eds Sickafus, K. E. & Kotomin, E. A.) Ch. 1 (Springer, NATO Publishing Unit, Dordrecht, The Netherlands, 2006).

Acknowledgements

The authors gratefully acknowledge support of this work by the General Motors/Brown Collaborative Research Laboratory on Computational Materials Science and the NSF Materials Research Science and Engineering Center on Micro and Nanomechanics of Materials at Brown University. W.A.C. thanks the John Simon Guggenheim Foundation for a fellowship, during which important components of this work were carried out, and C. Picu, B. Devincere and L. Kubin for discussions. Correspondence and requests for materials should be addressed to W.A.C.

Competing financial interests

The authors declare that they have no competing financial interests.

Reprints and permission information is available online at <http://npg.nature.com/reprintsandpermissions/>